minerals

MDPI

Article

In Situ Geochemical and Sr–Nd Isotope Analyses of Apatite from the Shaxiongdong Alkaline–Carbonatite Complex (South Qinling, China): Implications for Magma Evolution and Mantle Source

Jian Li [1,2], Chenyang Ye [1,2] and Jifeng Ying [1,2,*]

[1] State Key Laboratory of Lithospheric Evolution, Institute of Geology and Geophysics, Chinese Academy of Sciences, Beijing 100029, China; lijian16@mails.ucas.ac.cn (J.L.); yechenyang19@mails.ucas.ac.cn (C.Y.)
[2] College of Earth and Planetary Sciences, University of Chinese Academy of Sciences, Beijing 100049, China
* Correspondence: jfying@mail.iggcas.ac.cn

Abstract: We present in situ major element, trace element, and Sr–Nd isotope data of apatite from an alkaline–carbonatite intrusion in the South Qinling Belt (SQB) to investigate their magma evolution and mantle sources. The Shaxiongdong (SXD) complex consists predominantly of the early Paleozoic hornblendite, nepheline syenite, and subordinate Triassic carbonatite. Apatites from all lithologies are euhedral to subhedral and belong to fluorapatite. Elemental substitution varies from $REE^{3+} + Na^{+} + Sr^{2+} \leftrightarrow 3Ca^{2+}$ in carbonatite and syenite apatite to $Si^{4+} + 2Na^{+} + 2S^{6+} + 4REE^{3+} \leftrightarrow 4P^{5+} + 5Ca^{2+}$ in hornblendite apatite. Apatites are characterized by enriched rare earth elements (REEs) and depleted high field strength elements (HFSEs). They record the distinct evolution of their parental magmas. The weak, negative Eu anomaly in hornblendite apatite, together with the lack of Eu anomalies in the bulk rocks, indicates a relatively reduced magma. The Sr–Nd isotope data of the apatite in SXD carbonatite, falling on the East African carbonatite line (EACL) and close to the field of Oldoinyo Lengai carbonatite, indicate that the SXD carbonatite is derived from a mixed mantle source consisting of the HIMU component and subducted sedimentary carbonates. The similarity in Sr and Nd isotopic compositions between the SXD hornblendite and syenite apatites and the early Paleozoic mafic-ultramafic dykes in the SQB suggests that they may share a common metasomatized lithospheric mantle source.

Keywords: apatite; carbonatite; hornblendite; syenite; in situ Sr–Nd isotopes

check for updates

Citation: Li, J.; Ye, C.; Ying, J. In Situ Geochemical and Sr–Nd Isotope Analyses of Apatite from the Shaxiongdong Alkaline–Carbonatite Complex (South Qinling, China): Implications for Magma Evolution and Mantle Source. *Minerals* **2022**, *12*, 587. https://doi.org/10.3390/min12050587

Academic Editor: William L. Griffin

Received: 28 March 2022
Accepted: 4 May 2022
Published: 6 May 2022

Publisher's Note: MDPI stays neutral with regard to jurisdictional claims in published maps and institutional affiliations.

Copyright: © 2022 by the authors. Licensee MDPI, Basel, Switzerland. This article is an open access article distributed under the terms and conditions of the Creative Commons Attribution (CC BY) license (https://creativecommons.org/licenses/by/4.0/).

1. Introduction

Apatite, with a general formula of $Ca_5(PO_4)(OH, F, Cl)$, is widespread in various environments ranging from the Earth's surface to the lithospheric mantle [1]. It is a ubiquitous accessory mineral in most igneous, metamorphic, and sedimentary rocks [2]. Apatite can also become a rock-forming mineral in phosphorites and iron oxide-apatite deposits [3–5]. As the most abundant phosphate on Earth, apatite is a wonderful mineral to use to explore the global phosphorus cycle [6,7]. Also, apatite has been found in some lunar basalts, indicating that the volatile phase may play an essential role in the evolution of lunar magmatism [8–10].

Apatite generally has variable trace element contents due to numerous substitutions. It is classified as fluorapatite, chlorapatite and hydroxyapatite based on the different column anions (F, Cl, OH). Fluorapatite and hydroxyapatite are the most commonly occurring phosphorus-bearing minerals in igneous rocks. Numerous studies have shown that apatite has a strong affinity for the REEs due to extensive substitution of REEs [11–14]. There are two major substitution mechanisms at Ca and P sites: (1) REE^{3+} and Na^{+} substitute for Ca^{2+} and (2) REE^{3+} and Si^{4+} substitute for Ca^{2+} and P^{5+} [15–17]. As a major REE-bearing mineral

in igneous rocks, apatite fractionation leads to REE depletion in the residual melts [18]. Other elements, such as Mn, Sr, and S, are often incorporated into the apatite crystal structure by substitution [19]. The trace element contents of magmatic apatite are controlled by temperature, pressure, oxygen fugacity, coexisting minerals, and host magma composition [17,19–22]. Thus, apatite can be used to trace magmatic processes (e.g., AFC and magmatic degassing) [23,24] and may reflect the composition of its parental magma [25,26]. In igneous rocks that underwent metamorphism or metasomatism, magmatic apatite is modified with respect to shape and composition. The apatite of metasomatic/metamorphic origin always shows fractured and porous crystals with overgrowth rims. Numerous inclusions of monazite and xenotime usually occur in the metasomatic areas [3]. Low REEs, especially light REEs (LREEs), characterize the metasomatic apatite due to dissolution and transportation by liquid/melts [12,27]. Thus, apatite is also a reliable indicator for metasomatism and hydrothermal evolution.

Carbonatites generally occur in the company of various alkaline rocks, such as syenite, melilite, and phelinite. It has long been accepted that carbonatites and their spatially associated alkaline rocks are genetically related, with the former formed from the latter either by liquid immiscibility [28,29] or by fractional crystallization [30,31]. However, experiments verify that carbonatitic melts can also be generated directly from carbonated peridotite, eclogite, or even perlites [32–34]. Furthermore, there are some carbonatites, such as those in Eden Lake [35] and Tapira [36], which are genetically unrelated with their spatially accompanied alkaline rocks, further confirming that spatially accompanied carbonatite and alkaline rocks are not necessarily coeval and genetically related.

Located in the South Qinling Belt (SQB), China, the SXD alkaline–carbonatite complex comprises nepheline syenite, hornblendite, and minor carbonatite. Previous U–Pb dating work on zircons yielded an age of 441 Ma for the syenite and 430 Ma for the carbonatite, suggesting they are coeval and derived from a common parental magma [37–39]. However, using zircon as a geochronometer to date carbonatite is problematic, as the experiment confirmed that carbonatitic melts can only crystallize baddeleyite rather than zircon [40], and zircon in carbonatitic melts is unstable and can easily be dissolved and replaced by baddeleyite or diverse calcium zirconates [40,41]. Our recent Ar–Ar dating work on primary biotite from the carbonatite yielded a well-defined plateau age of 226 Ma (unpublished), implying that although closely spatially associated, the hornblende and syenite are not genetically related to the carbonatite; thus, zircons in carbonatite are most likely inherited from the surrounding alkaline rocks. The SXD complex is a potential Nb–REE deposit, mainly hosted in the carbonatite. The Nb forms pyrochlore and the REEs are mainly preserved in apatite and a variety of REE minerals, such as burbankite, bastnasite, etc.

Apatite is the common REE-rich mineral in carbonatite and accompanied alkaline rocks. It occurs from early magmatic to late hydrothermal stages. Thus, apatite is an effective tool for revealing magma evolution history, tracing REE mineralization, and exploring the relationship between carbonatite and its accompanied alkaline rocks [42]. In addition, the extremely high Sr and Nd contents in apatites from carbonatite and its silicate counterparts, effectively buffering potential crustal contamination, make them highly reliable in deciphering the nature of the mantle sources of their parental magmas.

Hitherto, magma evolution and mantle sources of the SXD complex are not well understood. In this contribution, we report in situ geochemical and Sr–Nd isotopic analyses of apatite from both the alkaline silicate and carbonatitic rocks from the SXD complex with an aim to constrain their magma evolution and mantle sources.

2. Geological Setting and Petrography

The Qinling orogenic belt (QOB), linking the Dabie-Sulu orogenic belt in the east and the Kunlun-Qilian orogen to the west (Figure 1a), is a composite collisional orogenic belt formed by the multi-stage collision of the South China (SCB) and North China (NCB) Blocks during the Paleozoic and Mesozoic [43–45]. The boundary between the SCB and the QOB lies along the Mianlue suture, whereas the Lingbao-Luanshan-Wuyang fault marks

the final suture between the NCB and the QOB. The QOB comprises the South Qinling Belt (SQB) and the North Qinling Belt (NQB), which were welded together along the Shangdan suture. The NQB is thought to be a part of the southern margin of the NCB, whereas the SQB is proposed to be the passive continental margin of the SCB before the opening of the Mianlue Ocean during the late early Paleozoic [43]. Early Paleozoic bimodal volcanic rocks indicate the initial spreading of the Mianlue Ocean. In the Triassic, northward subduction of the Mianlue ocean ultimately resulted in an amalgamation of the SQB and SCB [44]. A suite of mantle-derived mafic sills associated with the post-collision stage occurs in South Qinling [46].

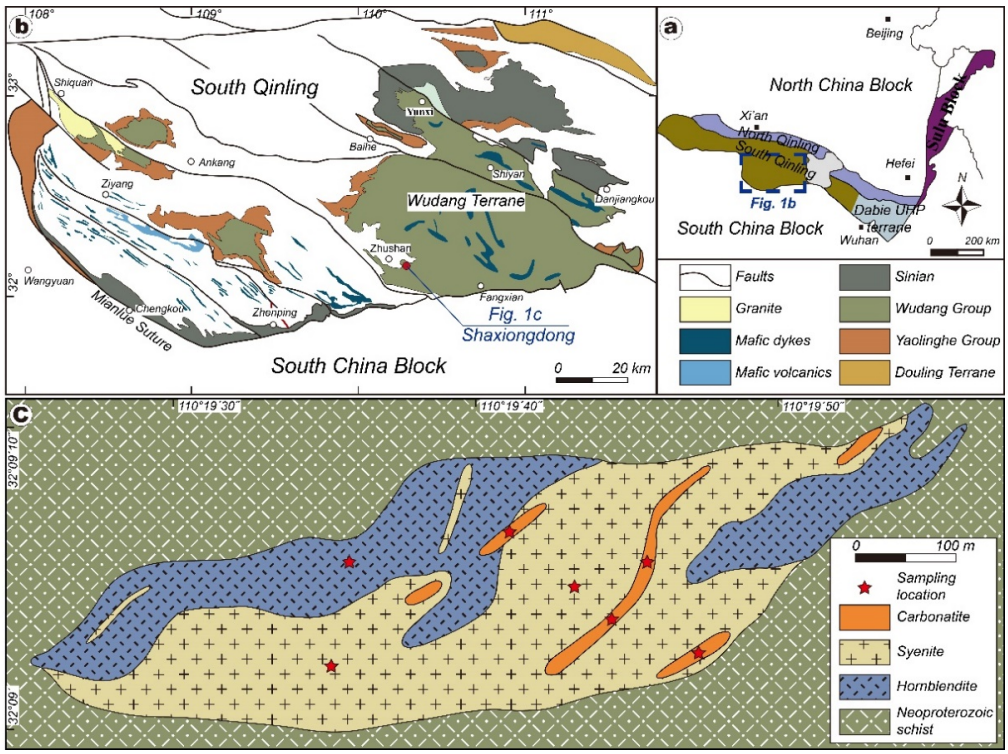

Figure 1. (**a**) Major tectonic units in Eastern China and the location of the South Qinling Belt; (**b**) simplified map showing the locality of the SXD complex within the South Qinling Belt (modified from [47]); (**c**) geological map of the SXD complex with the distribution of different lithologies.

The SQB is characterized by thin-skinned south-vergent imbricated thrust-fold systems. Two different Precambrian basements, namely the crystalline and transitional basements, have been distinguished in the SQB based on the lithology and metamorphic grade (Figure 1b). The crystalline basement is represented by amphibolite and granulite-facies assemblages of the Douling complex, whereas the transitional basement comprises the Meso-Proterozoic Yaolinghe and Wudang Groups of low-grade metamorphic volcano-sedimentary rock assemblages [45]. In addition, Neoproterozoic tillite and platform carbonate, Cambrian-Ordovician limestone, and Silurian shale unconformably overlie the basements.

The SXD alkaline–carbonatite complex, located around 12 km southeast of Zhushan County, Western Hubei Province, is tectonically situated at the southern margin of the Wudang terrane. It occurs as a spindle-like stock intruding on the Wudang Neoproterozoic metamorphic schist (Figure 1c). The complex is predominantly composed of the hornblendite outcropping in the northwestern and eastern parts of the intrusion and syenite in the central part. Subordinate carbonatite intruded on both syenite and hornblendite as dykes that are tens to hundreds of meters long. The carbonatite is medium-coarse grained and composed of medium- to fine-grained euhedral calcite (85%–95%), minor biotite (0%–10%), and aegirine (0%–5%). Accessory minerals include apatite, pyrochlore,

pyrite, barite, and REE minerals (e.g., bastnasite, burbankite, and allanite, Figure 2a–d). The nepheline syenite is fine- to medium-grained, porphyritic, and consists mainly of alkali feldspar (40%–75%), albite (5%–30%), nepheline (5%–15%), biotite (1%–5%), and aegirine (1%–5%). Accessory minerals include apatite, epidote, barite, zircon, and pyrite (Figure 2e). The hornblendite is medium-coarse grained, with modal amphibole approaching 80%–90%. Kaersutite occurs as the dominant phenocryst, whereas magnesiohastingsite and some Na–Ca amphibole (e.g., winchite) are present in the matrix. Subhedral phlogopite is another primary constituent mineral (~5%). Accessory minerals include ilmenite, magnetite, albite, titanite, apatite, wollastonite, rutile, and zircon (Figure 2f).

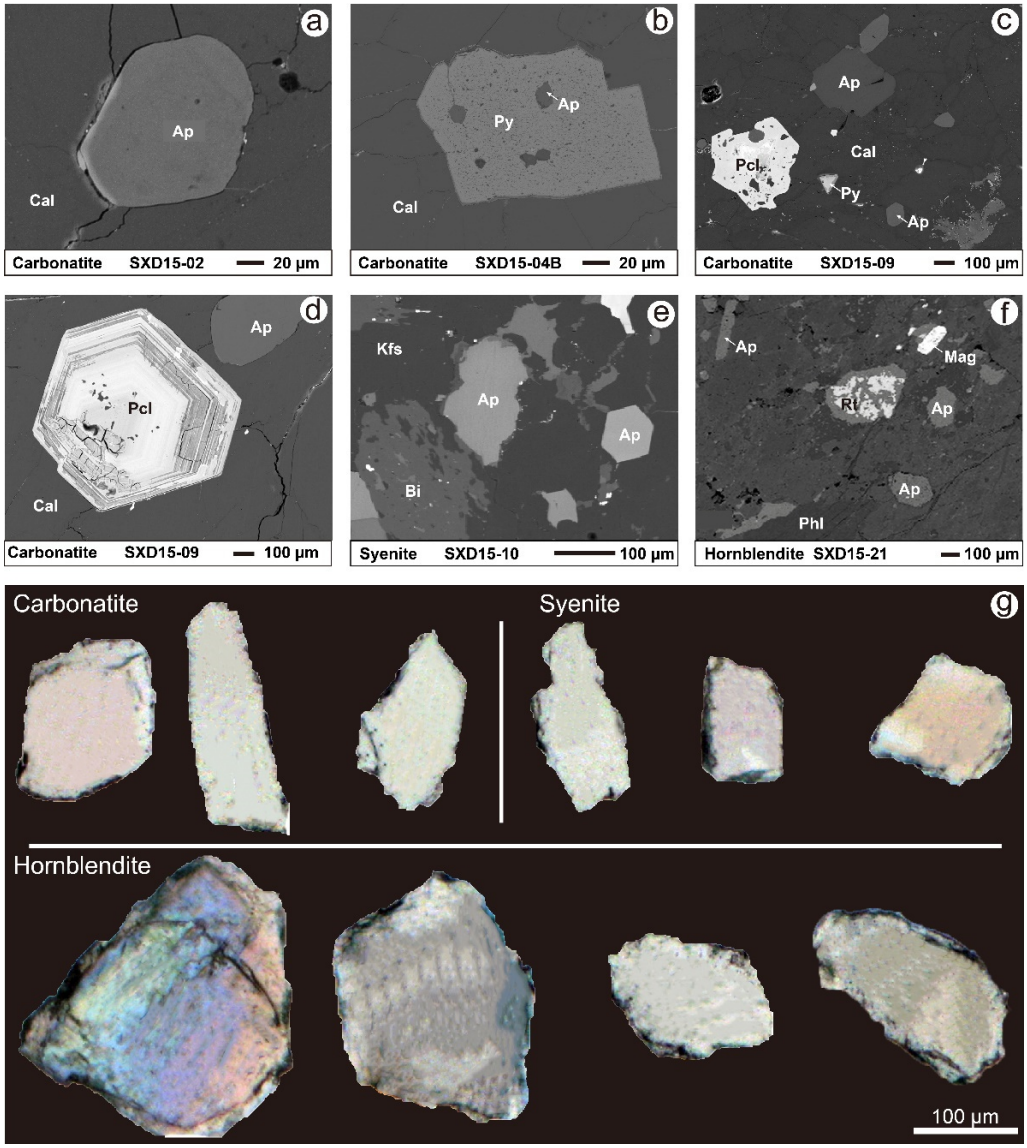

Figure 2. BSE of the SXD carbonatite (**a**–**d**), syenite (**e**), and hornblendite (**f**); and photomicrographs in transmitted light of representative apatite from the SXD complex (**g**). Symbols: Ap—apatite; Cal—calcite; Py—pyrite; Pcl—pyrochlore; Kfs—alkali feldspar; Bi—biotite; Mag—magnetite; Hbl—hornblende; Rt—rutile; Phl—phlogopite.

Apatites in the SXD complex mainly occur as euhedral–subhedral grains with typical hexagonal shapes (Figure 2). They are clear and homogeneous, as indicated by backscattered electron images (BSE), which contrast sharply with the porous apatite of metasomatic origin. Apatites from the carbonatite and syenite are commonly elongated or rounded with grain sizes of 80–300 μm. Those from hornblendite are relatively well-proportioned with

aspect ratios of 1–1.5 (Figure 2g). Fine anhedral apatite grains of 10–40 μm in size and enclosed in calcite and pyrite are commonly observed in the SXD carbonatite (Figure 2a,b). Some altered apatite-hosting monazite inclusions have also been reported [48].

3. Analytical Methods

Apatites were extracted separately from carbonatite, syenite, and hornblendite, following standard density and magnetic separation procedures. Apatite grains were then hand-picked, mounted in epoxy resin, and polished to expose the crystals' interiors. Polished mounts were then documented with photomicrographs before analyses to characterize apatite grains' crystal morphology (Figure 2g) and select targets for in situ elemental and Sr–Nd isotope analyses.

3.1. Major and Trace Elements

Major element compositions were measured using a JEOL-JAX8100 electron microprobe (EPMA) at the Institute of Geology and Geophysics, Chinese Academy of Sciences (IGGCAS), Beijing, China. The operating conditions were 15 kV accelerating voltage, 20 nA beam current, and 5 μm beam diameter. The standards for apatite analyses were apatite for Ca and P, albite for Na, diopside for Si, barite for S and Ba, celestine for Sr, monazite for La, Ce, Pr, and Nd, Mn oxide (MnO) for Mn, tugtupite for Cl, and synthetic fluorite for F. Apatite formulas were normalized to eight cations, assuming stoichiometry. Detection limits for analyzed elements ranged from ca. 100 ppm to 200 ppm.

Trace elements were determined on polished grain mounts of apatite by laser ablation inductively coupled plasma mass spectrometry (LA-MC-ICP-MS) equipped with a 193 nm excimer ArF LA system at the IGGCAS, with a 1 mm Ni sample cone and 0.4 mm Ni skimmer cone. The ablation cell was connected to an Agilent 77500a ICP-MS. Detailed instrument operation conditions, analytical procedures, and data reduction are described by Wu et al. [49]. To analyze these apatite grains, we used 40–60 μm laser craters pulsed at 6 Hz and an energy fluence of 6 J/cm^2. Dwell times were 10 ms for U and Th and 6 ms for isotopes of other elements; analyses involved ~30 s background acquisition and 50 s sample data acquisition, and helium was used as the carrier gas at 750 mL/ min. NIST 610 was used as the primary external calibration standard, and ^{43}Ca was used for internal calibration. Data were processed using the GLITTER program (GEMOC, Macquarie University). Relative analytical uncertainties were within 20% for Rb, Zr, Hf, and Ta, and 10% for other trace elements.

3.2. In Situ Sr and Nd Isotopic Composition

In situ Sr and Nd isotopic analyses of apatite were undertaken using a Thermo Scientific Neptune MC-ICP-MS and 193 nm excimer ArF LA system at the IGGCAS. The instrumental operation, analytical procedures, and data reduction are discussed in Yang et al. [50–52]. For Sr analysis, a laser repetition rate of 8 Hz with an energy fluence of 15 J/cm^2 was applied; the spot size was 80–120 μm. The influence of Ca on Sr isotope analysis was insignificant. The ^{87}Sr/^{86}Sr ratios obtained for in-house standard apatites AP1 and Slyudyanka were 0.711300 ± 0.000092 (2SD; n = 64) and 0.707752 ± 0.000010 (2SD; n = 44), respectively, consistent with their reference values [52].

With respect to the Nd isotope, a laser repetition rate of 6 Hz with an energy fluence of 15 J/cm^2 was applied with spot sizes of 90 μm. The influence of ^{142}Ce on ^{142}Nd was insignificant, so the main isobaric interference for Nd was that of ^{144}Sm on ^{144}Nd, which was corrected with a procedure similar to that of McFarlane et al. [53]. The ^{147}Sm/^{144}Nd and ^{143}Nd/^{144}Nd ratios obtained for in-house standard apatites MAD and Otter Lake were 0.082703 ± 0.000091 (2SD; n = 64) and 0.511348 ± 0.0000054 (2SD; n = 95), and 0.08472 ± 0.00039 and 0.511955 ± 0.0000064, respectively, which are identical to values obtained by solution methods and long-term determinations by LA-MC-ICP-MS [52,54].

4. Results

4.1. Major and Trace Elements

Apatite grains from the SXD complex have uniform CaO (49.9–57.0 wt%) and P_2O_5 (39.8–42.7 wt%), high F (2.9–5.0 wt%), and are typical fluorapatite (Table 1 and Supplementary Materials S1). Apatites in SXD carbonatite and syenite are high in SrO (0.29–2.2 wt%) and Na_2O (0.09–0.56 wt%), whereas those in SXD hornblendite have relatively low Na_2O (0.03–0.17 wt%) and high SiO_2 (0.07–0.4 wt%) and SO_3 (0.09–0.52 wt%). BaO, MnO, and Cl in most analyzed spots are below the detection limits, and SrO in apatite grains from SXD hornblendite is below the detection limit. All apatites are enriched in LREEs relative to heavy rare earth elements (HREEs), with $(La/Yb)_N$ ratios of 17–171, 16–64, and 20–45 for those in carbonatite, syenite, and hornblendite, respectively (Table 2 and Supplementary Materials S2, Figure 3a,c,e). In addition, apatites in SXD hornblendite show a discernable weak negative Eu anomaly (δEu = 0.73–0.95) [$\delta Eu = Eu_N / (Sm_N + Gd_N)^{1/2}$]. In the primitive mantle-normalized trace element diagrams (Figure 3b,d,f), all apatites show enrichment of Th and LREEs, and depletion of HFSEs, such as Nb-Ta, Zr-Hf, and Ti.

Table 1. Average apatite compositions obtained by EPMA.

Sample	SXD15-02	SXD15-04B	SXS15-09	SXD15-26	SXD15-08	SXD15-10	SXD15-21
Lithology		**Carbonatite**			**Syenite**		**Hornblendite**
Composition	**(*n* = 10)**	**(*n* = 10)**	**(*n* = 7)**	**(*n* = 10)**	**(*n* = 8)**	**(*n* = 10)**	**(*n* = 10)**
CaO	53.13	52.93	52.97	53.44	51.57	52.45	55.78
Ce_2O_3	0.45	0.36	0.23	0.32	0.60	0.30	0.09
La_2O_3	0.25	0.16	0.10	0.13	0.26	0.12	0.06
SrO	0.58	1.12	1.88	1.03	1.89	1.62	b.d.l.
BaO	b.d.l.	0.02	b.d.l.	0.02	b.d.l.	b.d.l.	b.d.l.
Na_2O	0.33	0.25	0.15	0.21	0.37	0.21	0.11
Pr_2O_3	b.d.l.	0.03	0.03	0.03	0.05	0.02	0.04
Nd_2O_3	0.06	0.12	0.07	0.19	0.30	0.08	b.d.l.
P_2O_5	40.97	41.17	41.42	41.52	41.14	41.70	41.64
SiO_2	0.11	0.05	0.01	0.04	0.01	0.01	0.20
SO_3	0.11	0.07	0.06	0.04	0.08	0.08	0.27
MnO	b.d.l.	b.d.l.	b.d.l.	b.d.l.	b.d.l.	b.d.l.	b.d.l.
F	3.55	3.97	4.24	3.70	4.06	3.70	3.42
Cl	b.d.l.	b.d.l.	b.d.l.	b.d.l.	b.d.l.	b.d.l.	b.d.l.
$-O=(F, Cl)_2$	1.50	1.65	1.81	1.54	1.65	1.56	1.43
total	98.09	98.61	99.36	99.14	98.67	98.74	100.21
in apfu			Structural formula calculated for 8 cations				
Ca	4.89	4.88	4.86	4.89	4.78	4.83	5.00
Na	0.06	0.04	0.03	0.04	0.06	0.04	0.02
Sr	0.03	0.06	0.09	0.05	0.09	0.08	—
Ba	—	0.00	—	0.00	—	—	—
La	0.01	0.00	0.00	0.00	0.01	0.00	0.00
Ce	0.01	0.01	0.01	0.01	0.02	0.01	0.00
Pr	—	0.00	0.00	0.00	0.00	0.00	0.00
Nd	0.00	0.00	0.00	0.00	0.01	0.00	—
P	2.98	3.00	3.00	3.00	3.02	3.04	2.95
Si	0.01	0.00	0.00	0.00	0.00	0.00	0.02
S	0.01	0.00	0.00	0.00	0.00	0.00	0.02
Mn	—	—	—	—	—	—	—
F	0.97	1.08	1.15	1.00	1.11	1.01	0.90
Cl	—	—	—	—	—	—	—

Notes: b.d.l., below the detection limit; —, no data.

Table 2. Average apatite trace element concentrations obtained by LA-MC-ICP-MS.

Sample	SXD15-02	SXD15-04B	SXS15-09	SXD15-26	SXD15-08	SXD15-10	SXD15-21
Lithology	Carbonatite				Syenite		Hornblendite
	(*n* = 10)	(*n* = 10)	(*n* = 8)	(*n* = 10)	(*n* = 10)	(*n* = 10)	(*n* = 10)
Sc	3.38	8.64	6.75	6.75	7.10	3.58	7.84
Ti	28.6	63.6	59.4	59.4	61.7	28.9	55.5
V	25.7	6.80	4.42	4.42	5.40	2.40	68.4
Cr	47.4	109	88.0	88.0	88.3	52.0	100.0
Mn	344	338	412	412	644	563	321
Fe	297	715	500	500	531	425	795
Co	7.91	18.5	14.0	14.0	14.3	8.23	16.5
Ni	16.4	39.6	29.2	29.2	28.1	16.9	34.1
Rb	0.72	1.37	1.33	1.33	1.21	0.76	1.46
Sr	12,671	15,997	24,873	24,873	22,815	21,857	1629
Y	354	480	488	488	937	846	199
Zr	1.11	2.24	1.85	1.85	1.96	1.04	13.7
Nb	0.97	0.59	0.37	0.37	0.36	0.27	0.44
Cs	0.15	0.33	0.24	0.24	0.22	0.13	0.34
Ba	27.3	20.7	65.6	65.6	9.09	18.4	5.81
La	1373	1078	950	950	1551	796	498
Ce	3204	3011	2584	2584	4634	2396	963
Pr	410	417	352	352	633	348	116
Nd	1789	1924	1618	1618	2986	1695	518
Sm	349	398	383	383	689	467	98.3
Eu	105	118	126	126	223	161	24.1
Gd	251	291	324	324	548	420	78.8
Tb	28.3	34.9	40.7	40.7	69.4	57.5	9.58
Dy	117	151	176	176	305	267	47.4
Ho	15.9	20.9	24.0	24.0	43.0	38.6	7.72
Er	27.2	36.9	40.2	40.2	76.2	69.3	16.3
Tm	2.45	3.38	3.42	3.42	6.96	6.56	1.78
Yb	10.9	14.4	14.1	14.1	29.4	28.0	9.87
Lu	1.05	1.36	1.20	1.20	2.68	2.59	1.21
Hf	0.25	0.64	0.44	0.44	0.43	0.29	0.51
Ta	0.05	0.08	0.07	0.07	0.08	0.06	0.09
Th	13.6	15.0	10.1	10.1	23.8	14.1	16.5
U	0.31	0.11	0.08	0.08	0.16	0.16	2.74
Pb	9.61	19.0	18.4	18.4	22.7	20.9	27.4

4.2. Sr and Nd Isotopic Composition

The Sr–Nd isotopic compositions of apatite are listed in Table 3 and Supplementary Materials S3. The initial isotopic ratios of the apatites in the SXD carbonatite are calculated back to 220Ma based on our unpublished dating results of biotite, yielding initial $^{87}Sr/^{86}Sr$ ratios of 0.70202–0.70332 and $\varepsilon_{Nd}(t)$ values of 0.6–3.4 (Figure 4a). For SXD hornblendite and syenite, the initial Sr and Nd isotopic ratios were recalculated based on the zircon U–Pb age (435 Ma, our unpublished data). The initial $^{87}Sr/^{86}Sr$ and $\varepsilon_{Nd}(t)$ are 0.70301–0.70333 and 1.5–3.8, and 0.70337–0.70389 and 2.5–6.2 for hornblendite and syenite apatite, respectively (Figure 4b).

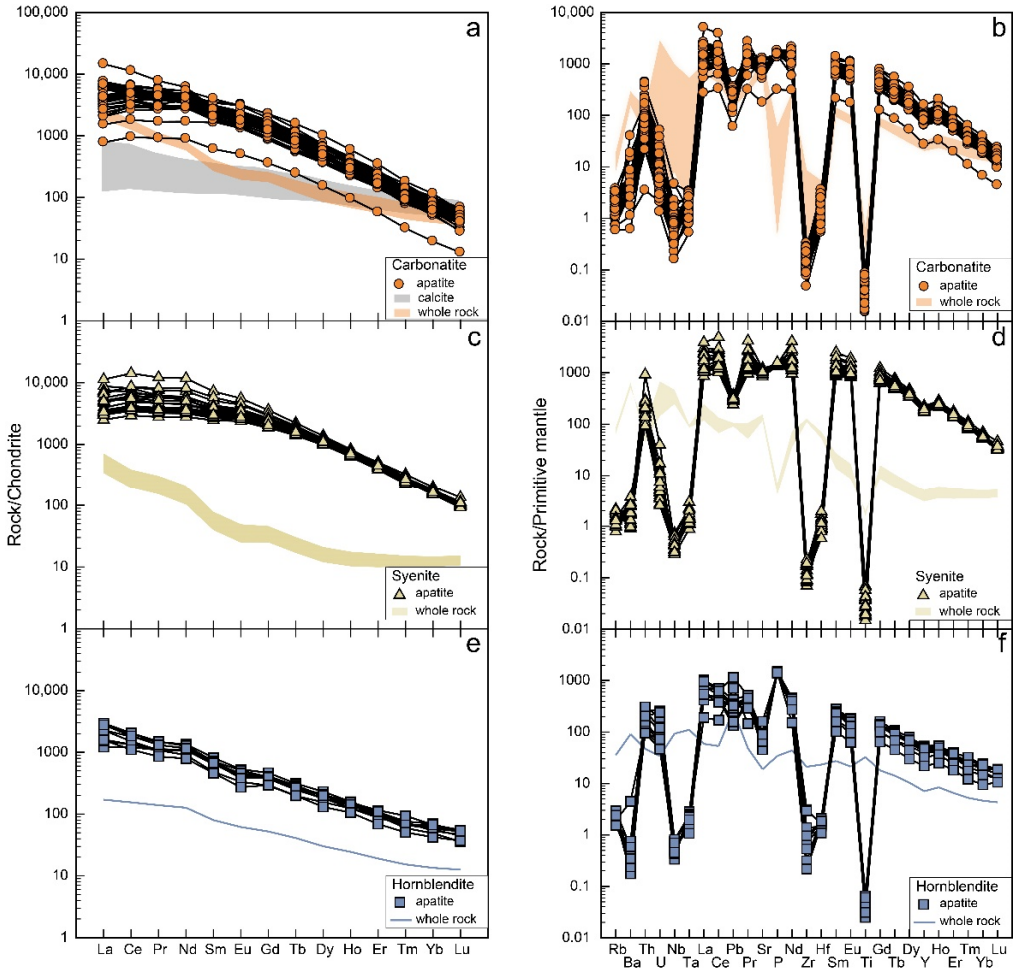

Figure 3. Chondrite-normalized REE patterns (**a**,**c**,**e**) and primitive mantle-normalized trace element diagrams (**b**,**d**,**f**) of the SXD carbonatite, syenite, and hornblendite. Chondrite and primitive mantle values are from Anders and Grevesse [55] and Sun and McDonough [56], respectively. The REE data of calcite are from Xu et al. [37] and Chen et al. [38].

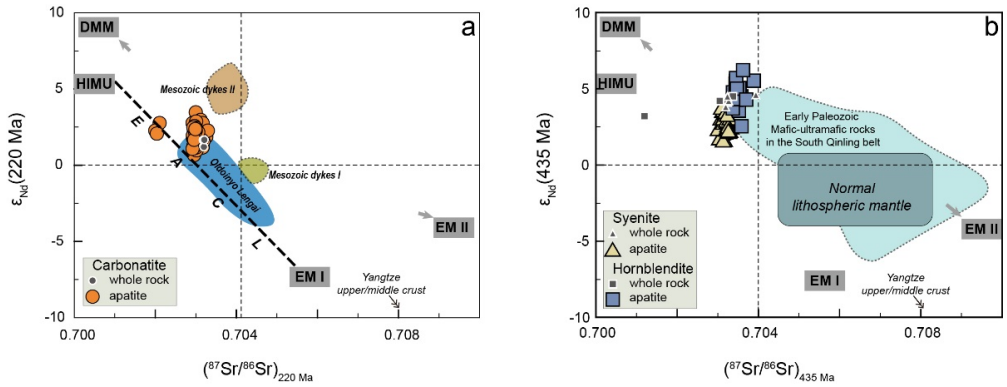

Figure 4. Sr–Nd isotopic diagram for the SXD Triassic carbonatite (**a**) and early Paleozoic hornblendite–syenite intrusion (**b**). The data of Mesozoic dykes are from Nie et al. [46]. The East African carbonatite line (EACL) and Oldoinyo Lengai are referred to in [57–59]. The normal lithospheric mantle is constrained by the Early Paleozoic mafic dykes in South Qinling [60,61]. The Yangtze upper/middle crust data are from Chen and Jahn [62], Gao et al. [63], and Ma et al. [64]. The data of the early Paleozoic mafic-ultramafic rocks in the South Qinling Belt are from [65].

Table 3. Average apatite Sr–Nd isotope data obtained by LA-MC-ICP-MS.

Sample	Lithology		$^{87}Rb/^{86}Sr$	2σ	$^{87}Sr/^{86}Sr$	2σ	$(^{87}Sr/^{86}Sr)i$	2σ	$^{147}Sm/^{144}Nd$	2σ	$^{143}Nd/^{144}Nd$	2σ	$\varepsilon_{Nd}(T)$	2σ	TDM(Ma)	2σ
													ε_{Nd}(220 Ma)			
SXD15-02	Carbonatite	(*n* = 20)	0.00002	0.00001	0.70308	0.00006	0.70308	0.00006	0.10983	0.00044	0.51262	0.00003	2.1	0.6	784	45
SXD15-04B		(*n* = 19)	0.00001	0.00001	0.70300	0.00005	0.703	0.00005	0.13221	0.00009	0.51264	0.00004	1.9	0.8	959	73
SXS15-09		(*n* = 18)	0.00001	0.00001	0.70302	0.00004	0.70302	0.00004	0.13986	0.00019	0.51264	0.00004	1.6	0.7	1080	76
SXD15-26		(*n* = 20)	0.00003	0.00001	0.70299	0.00006	0.70299	0.00006	0.12417	0.00052	0.51264	0.00003	2	0.6	912	61
													ε_{Nd}(435 Ma)			
SXD15-08	Syenite	(*n* = 15)	0.00003	0.00001	0.70313	0.00005	0.70313	0.00005	0.15269	0.00035	0.51264	0.00003	2.6	0.5	1296	73
SXD15-10		(*n* = 20)	0.00002	0.00001	0.70326	0.00004	0.70326	0.00004	0.16826	0.00016	0.51269	0.00003	2.6	0.7	1586	118
SXD15-21	Hornblendite	(*n* = 20)	0.00149	0.00012	0.70351	0.00003	0.70351	0.00003	0.12192	0.00021	0.51266	0.00009	4.6	1.8	817	153
AP1	Standard	(*n* = 64)	0.00007	0.000006	0.711300	0.000092										
Slyudyanka		(*n* = 44)	0.000006	0.000004	0.707752	0.000010										
MAD		(*n* = 95)							0.082703	0.000091	0.511348	0.0000054				
Otter Lake		(*n* = 44)							0.08472	0.00039	0.511955	0.0000064				

5. Discussion

5.1. Origin of the Apatite: Magmatic or Metasomatic?

Apatite, which occurs throughout early-stage magmatic to late-stage hydrothermal environments, has distinct morphology and geochemical signatures [66]. Apatite of magmatic origin is generally euhedral to subhedral with or without zoning textures [18,21]. They typically contain F as the dominant volatile species over Cl and H_2O [67]. Apatites in various kinds of host igneous rocks are highly diverse in terms of trace element composition [1,19,27]. For example, apatites in granite are characterized by a strong negative Eu anomaly, resulting mainly from plagioclase crystallization [68,69]. As the common REE-enriched mineral in carbonatite, alkaline, mafic, and ultramafic rocks, apatite is enriched in LREEs with high $(La/Yb)_N$ and Sr/Y ratios, corresponding to the right-sloping patterns in the chondrite-normalized REE diagram [18,21,27]. Metasomatic apatites usually show turbid cores and overgrowth rims with abundant inclusions of xenotime and monazite. They have relatively lower REE concentrations. The preferential transport of the LREEs away from the original apatite leads to passive enrichment of HREEs in the metasomatic apatites, leaving low $(La/Yb)_N$ ratios and flat or even left-sloping patterns in the chondrite-normalized REE diagram [3,12,48]. Hydrothermal apatites occur as fine anhedral grains and show association with baryte, fluorite, and REE minerals (e.g., synchysite and monazite). Their REE patterns are highly variable [18,70–74] due to the control of REE transport and fractionation by REE complexes of CO_2 and saline (chloride or fluoride) in hydrothermal fluids [75–79].

As shown in Figure 2a,b, the apatite (<50 μm) from the SXD carbonatite occurs as fine anhedral inclusions in calcite and pyrite, suggesting that apatite can crystallize at early magmatic stages. The apatite grains studied are euhedral to subhedral (>80 μm) with a well-formed crystal shape (Figure 2g), irrespective of lithology. They have clear cores and lack monazite inclusions. They are all typical fluorapatite as evidenced by high F and undetected Cl contents. They are enriched in REEs and have high Sr/Y ratios (Figure 5a), indicative of magmatic origin and little or no metasomatic influence [27]. They have high $(La/Sm)_N$ and $(La/Yb)_N$ ratios, falling into the field of magmatic apatite and showing a sharp contrast with the altered apatites from the SXD complex (Figure 5b) [48,70]. Moreover, altered apatites are usually characterized by inclusions of xenotime and monazite [48], which is not the case for the apatites we studied. In addition, they also show similar compositions with the magmatic apatite of corresponding rock types (Figure 5c–e). The Sr and Nd isotopic compositions of the apatites are homogenous. They overlap those of their host rocks (Figure 4), indicating that the apatite had been fractionally crystallized from the host magma that had evolved in a closed system. Trace element abundances of the magmatic apatite are mainly controlled by partition coefficients, geochemistry of the host magma, and crystallization phases simultaneous to or before the apatite. Thus, their geochemical signatures are used to decipher the evolution of the parental magmas and the nature of their mantle sources.

5.2. Constraining Magma Evolution by Apatite Composition

5.2.1. Carbonatite

Apatite is the primary REE-bearing accessory mineral in carbonatite. Previous studies have demonstrated that REE substitutes on the Ca site accompanied by Na substitution on the Ca site or Si substitution on the P site can compensate for charge excess [15,17,19,83]. The apatite from the SXD carbonatite shows low Ba, Si, S, and Mn contents, and there is no apparent correlation between them. By contrast, Na, Sr, and LREEs correlate well with the P and Ca (Figure 6a). In general, these elements are preferred to substitute for Ca [15–17]. Thus, the substitution formula is likely to be:

$$REE^{3+} + Na^{+} + Sr^{2+} \leftrightarrow 3Ca^{2+} \quad (1)$$

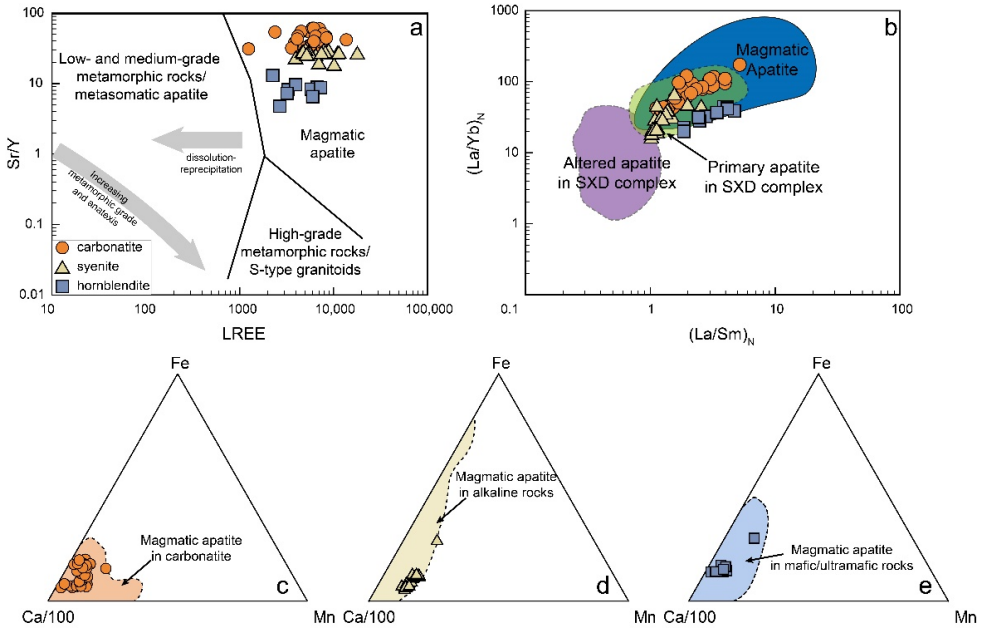

Figure 5. Sr/Y vs. LREEs (modified after O'Sullivan et al. [27]) (**a**), $(La/Sm)_N$ vs. $(La/Yb)_N$ diagram for the SXD apatites (**b**), and comparison of apatite composition from carbonatite (**c**), alkaline rocks (**d**), and mafic/ultramafic rocks (**e**). The data of magmatic apatite are from [18,21,42,48,70,80–82] and references therein. The primary and altered apatite in the SXD complex are referred to in [48,70]. Data for apatite in carbonatite, alkaline rock, and mafic/ultramafic rocks are from [21] and references therein.

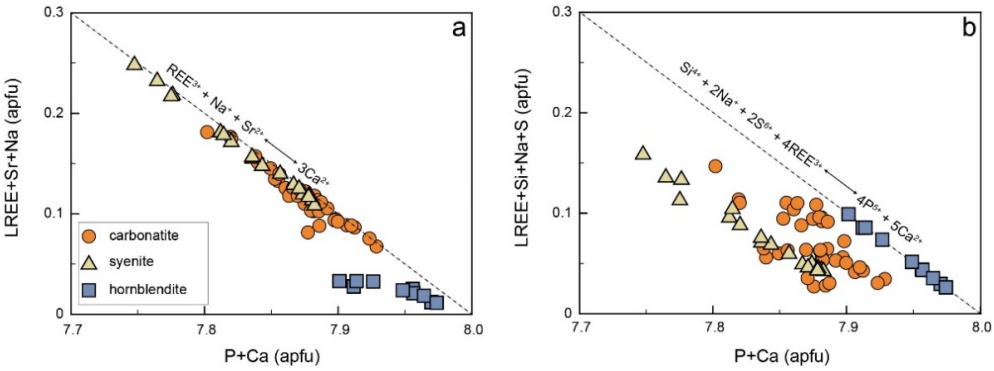

Figure 6. Elemental substitution mechanisms for apatites in SXD complex. Correlations of (Ca + P) with (**a**) (LREE + Sr + Na) and (**b**) (LREE + Si + Na + S).

The apatites in SXD carbonatite show high total REE contents (up to 15000 ppm). Experimental results reveal that REEs are moderately incompatible in apatite in the pure carbonatitic melt without silica contents [84], and their compatible behaviors are independent of temperature, pressure, or volatiles [84,85]. However, increasing evidence demonstrates that the addition of silica elevates the polymerization of the carbonatite melt, which significantly enhances the partition coefficients of REEs between apatite and melt by means of facilitating the entry of REEs into the Ca site of apatite [13,18,42,86,87]. It is clear that the SXD carbonatite is not pure, as evidenced by the whole-rock SiO_2 content of 2.7% on average and the occurrence of modal silicate minerals, such as biotite. So, the high REE contents in SXD carbonatite apatite can be reasonably accounted for by the elevated silica in the SXD carbonatite.

As a result of fractionation of REE-enriched apatite, the residual melt should be depleted of REEs and have a lower enrichment of La with respect to Nd (i.e., LREE/HREE) [18], which is consistent with the relatively flat chondrite-normalized REE patterns of the calcite

(Figure 3a) [37,38]. In addition, $(La/Yb)_N$ and Th are positively correlated with LREEs (Figure 7a,c), which is probably due to the crystallization of pyrochlore or allanite in magma, as both are enriched in LREEs. The difference between allanite and pyrochlore is that the former is strongly enriched in Th over U. Therefore, the crystallization of allanite would lead to an extreme depletion of Th with a slight decrease of U in the residual melt [88]. In the case of SXD carbonatite, apatite displays extremely low U (~0.1 ppm) but variable Th (0.3–37 ppm) [85], which precludes allanite as a significant crystallization phase. Pyrochlore is the dominant Nb-bearing accessory mineral in the SXD carbonatite. Its euhedral hexagonal crystal shape suggests that it crystallized during early-stage magmatism. As pyrochlore usually has high U (>1300 ppm) and Th (>200 ppm) contents [38], crystallization of pyrochlore would decrease Nb, Th, U, and LREE contents in the residual melt, consistent with the strong negative Nb anomaly of apatite and calcite (Figures 3b and 7c,d) [37,38].

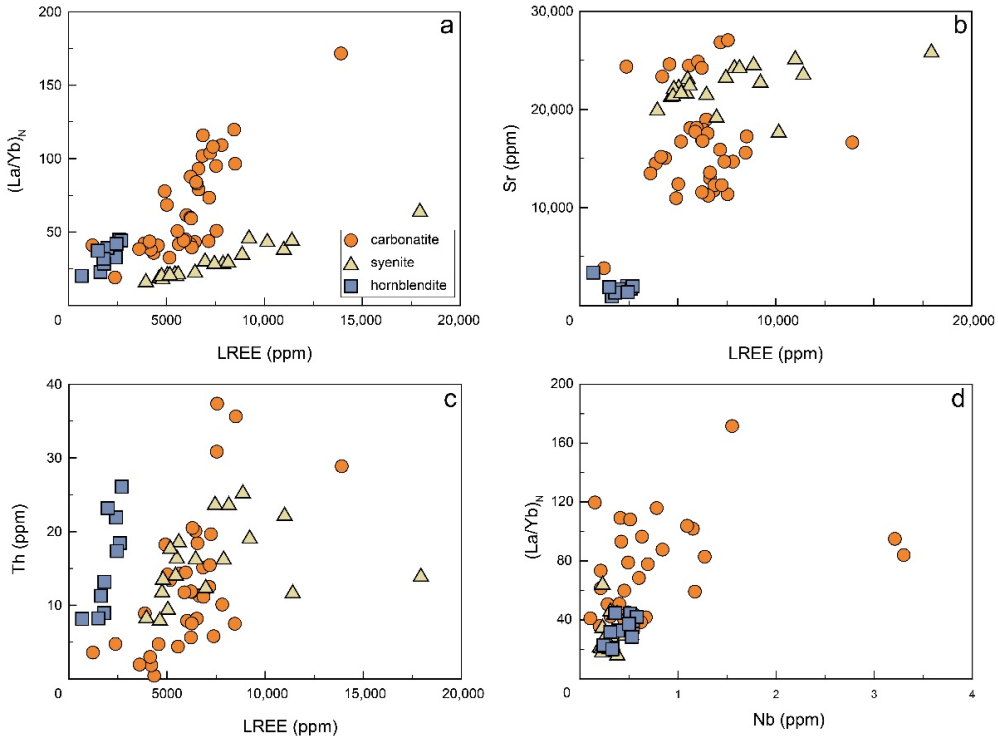

Figure 7. Variation diagrams of LREEs with (**a**) $(La/Yb)_N$, (**b**) Sr, (**c**) Th, and (**d**) Nb vs. $(La/Yb)_N$ for the apatites in SXD complex.

5.2.2. Syenite

The apatites from the SXD syenite have high Na_2O, SrO, and LREEs (Figure 6a), which are preferred to substitute for Ca [15–17], and the substitution formula may be:

$$REE^{3+} + Na^{+} + Sr^{2+} \leftrightarrow 3Ca^{2+} \quad (2)$$

The relatively high Na_2O contents of apatites suggest that they should have crystallized from a Na-rich magma [87], which is consistent with the high Na_2O (8.8–9.8 wt%) of their host syenite. Experimental studies reveal that the REEs are compatible in apatite crystallizing from silicate melts, and middle REEs (MREEs) usually have higher partition coefficients than LREEs and HREEs ($^{ap/liq}D_{MREE} > {}^{ap/liq}D_{LREE}$ or $^{ap/liq}D_{HREE}$) [83,87,89]. This is consistent with the concave-downward REE patterns of the apatite from the syenite (Figure 3c). The extremely low Zr, Hf, and U contents compared with the host syenite are indicative of the coeval crystallization of zircon. Generally, the partitioning of Sr between apatite and silicate melt is relatively constant and insensitive to changes in temperature, pressure, volatiles, or melt composition. Thus, the positive correlation between LREE and Sr contents (Figure 7b) suggests that the partition coefficients of REEs are relatively constant

as well. Therefore, the positive correlation between LREEs and $(La/Yb)_N$ (Figure 7a) is likely attributed to the crystallization of LREE-rich minerals, such as monazite and allanite. As allanite is enriched in Th and LREEs, its crystallization would decrease LREEs and Th in the melt. Thus, the decrease of LREEs with decreasing Th (Figure 7c) shown by the apatite in syenite points to a potential coeval crystallization of allanite rather than monazite, which is also consistent with the absence of monazite in SXD syenite.

5.2.3. Hornblendite

The apatites from the hornblendite have relatively high Na, Si, and S, but low Sr contents. They show an insignificant correlation between P + Ca and REE + Na, indicating a different substitution mechanism from those in apatite for both carbonatite and syenite (Figure 6a). There is a perfect negative correlation between P + Ca and REE + Si + S + Na (Figure 6b) and a positive correlation between S + REE and Si and Na. Thus, the substitution for the apatite from the SXD hornblendite is likely to be:

$$Si^{4+} + 2Na^{+} + 2S^{6+} + 4REE^{3+} \leftrightarrow 4P^{5+} + 5Ca^{2+} \quad (3)$$

It has been well demonstrated that apatite from most mafic rocks shows smooth or concave-downward REE patterns due to the high partition coefficients of MREEs [27,90,91]. Apatites from the SXD hornblendite exhibit weak concave-upward REE patterns with slight negative Eu anomalies (δEu = 0.73–0.95, Figure 8). They usually occur interstitially, implying crystallization later than the cumulus amphibole. Since the amphibole is invariably characterized by higher MREE partition coefficients relative to the LREEs and HREEs, their cumulate would leave an MREE-decreased residual melt, from which the apatite crystallized subsequently. That may be the main cause of the weak concave-upward chondrite-normalized REE patterns in the SXD hornblendite apatite (Figure 3e). The SXD hornblendite whole rock has a negligible Eu anomaly (0.96) compared to the apatite. As there is no plagioclase in the SXD hornblendite, the negative Eu anomaly of apatite is not caused by plagioclase fractionation. Ce and Eu generally have two ionic valences each: Ce^{3+}, Ce^{4}, Eu^{2+}, and Eu^{3+}. Ce^{3+} and Eu^{3+} preferentially substitute for Ca^{2+} in apatite due to their similar ionic radii [15,16,19,92]. Therefore, the weak negative correlation between δEu and δCe most likely indicates more Ce^{3+} and Eu^{2+} relative to Ce^{4+} and Eu^{3+} in the host magma, suggesting that magma evolution of SXD hornblendite may have proceeded under relatively reduced conditions (Figure 8) [93]. Calcic amphibole (kaersutite and magnesiohastingsite) may incorporate more Eu^{2+}, as their Ca^{2+} has a similar ionic radius with that of Eu^{2+} [94–97].

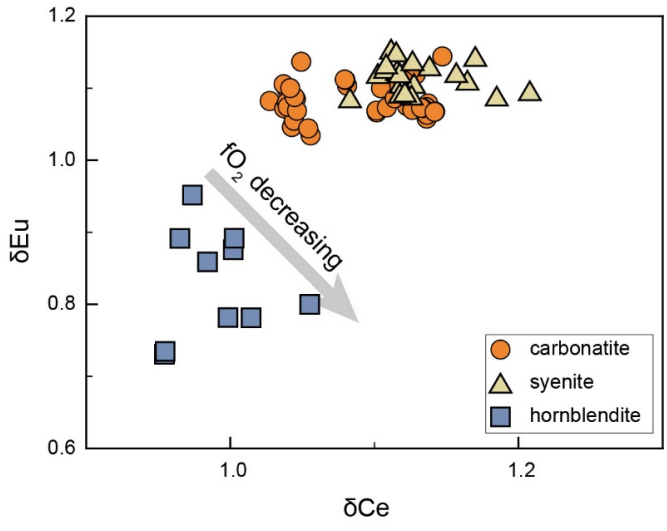

Figure 8. δCe vs. δEu plot for the apatite in SXD hornblendite.

5.3. Implication for the Mantle Source

The magmatic apatites from the SXD complex show Sr–Nd isotopic compositions overlapping with their host rocks, arguing for magma evolution in a closed system. Thus, the isotopic ratios of apatites are representative of their mantle sources.

During the early Paleozoic, the SQB was in a rift setting, as evidenced by widespread collapsed basins, faults, and rift-related igneous rocks [43,45]. Numerous mafic dykes and sills of similar age to the SXD hornblendite and syenite are widely distributed in the North Daba Mountains, Wudang terrane, and Suizao area [65,98]. They are all of the alkaline affinity and are characterized by OIB-like trace element signatures [61,98,99]. The Sr–Nd–Pb isotopic compositions reveal that their mantle source follows a mixing trend between DMM/HIMU and EM (EMI, EMII, or both) components [99]. Accumulating geochemical evidence and studies of pyroxenite-hornblendite xenoliths further point to a metasomatic lithospheric mantle [46,100–102]. Considering the geochemical similarity, especially the similar Sr and Nd isotopic compositions between the SXD hornblendite and syenite and the early Paleozoic mafic-ultramafic rocks in the SQB (Figure 4b), it is reasonable to postulate that the SXD hornblendite and syenite may share a common metasomatic lithospheric mantle source with these early Paleozoic mafic-ultramafic rocks.

Carbonatite is considered the product of low-degree partial melting of the mantle and is commonly associated with extensional settings [103]. Thus, the formation of SXD carbonatites most likely suggests a shift from a compressional to a post-collision extensional regime at ca. 220Ma. There are two types of Triassic mafic dykes occurring in the Wudang terrane and they are considered to be derived from the asthenosphere (Mesozoic dyke II in Figure 4b) and a mixed mantle source between the asthenosphere and subducted crustal material (Mesozoic dyke I in Figure 4b), respectively [46]. It is clear that the SXD carbonatite is different from these two types of dykes in terms of Sr and Nd isotopic compositions, implying a highly heterogeneous mantle beneath the SQB during the Triassic. The Sr–Nd isotopic compositions of the apatite in SXD carbonatite fall into the field defined by Oldoinyo Lengai carbonatite and on the East African carbonatite line (EACL), which are considered to be connected to the HIMU and EM I mantle components [57–59]. Diverse components have been proposed to account for the HIMU signature, such as the recycled basaltic oceanic crust [104], metasomatic lithospheric mantle [105,106] or Archean to early Proterozoic subduction-related carbonatite-metasomatized sub-continental lithospheric mantle [107–109]. In the SXD case, however, the carbonatite has a lighter Mg isotopic composition than the normal mantle (our unpublished data), unequivocally demonstrating the involvement of recycled carbonate in its mantle source. Considering the diffusion coefficient of the Mg isotope in inter-mineral systems [110,111], the recycled crustal materials of Archean or Proterozoic would be re-equilibrated with the surrounding mantle. Thus, we propose that sedimentary carbonates, subducted following the final closure of the Mianlue ocean and subsequent amalgamation of the SQB and SCB in the Triassic, would be the proper candidates to account for the light-Mg isotope signature. Therefore, we propose that the SXD carbonatite may be derived from a mixed mantle source of HIMU components and subducted sedimentary carbonates.

6. Conclusions

1. Apatites from the SXD complex are of magmatic origin and have not experienced subsequent metasomatism or other alteration. Their Sr–Nd isotopic compositions that overlap with host rocks indicate magma evolution in a relatively closed system with no significant crustal contamination.
2. The major elemental substitution mechanism in apatite from SXD carbonatite is $REE^{3+} + Na^{+} + Sr^{2+} \leftrightarrow 3Ca^{2+}$, whereas those for apatites in syenite and hornblendite are $REE^{3+} + Na^{+} + Sr^{2+} \leftrightarrow 3Ca^{2+}$ and $Si^{4+} + 2Na^{+} + 2S^{6+} + 4REE^{3+} \leftrightarrow 4P^{5+} + 5Ca^{2+}$, respectively.
3. Pyrochlore crystallization plays an important role in controlling the REE signature of apatite from the carbonatite, while the fractionation of zircon, allanite, and amphi-

bole from the magma significantly affects the geochemistry of apatites from syenite and hornblendite.

4. The early Paleozoic hornblendite and syenite are derived from a metasomatic lithospheric mantle. In contrast, their Triassic carbonatitic counterpart is derived from a mixed mantle source consisting of HIMU components and recycled sedimentary carbonates.

Supplementary Materials: The following supporting information can be downloaded at: https://www.mdpi.com/article/10.3390/min12050587/s1, Supplementary Materials S1: Apatite major elements obtained by EPMA; Supplementary Materials S2: In situ trace elements (ppm) of apatite grains in the SXD complex; Supplementary Materials S3: In situ Sr and Nd isotopic compositions of apatite grains in the Shaxiongdong complex by LA-MC-ICP-MS.

Author Contributions: Conceptualization, J.L. and J.Y.; methodology, J.Y.; software, J.L.; validation, J.L., C.Y. and J.Y.; formal analysis, J.L.; investigation, J.L., C.Y. and J.Y.; resources, J.Y.; data curation, C.Y.; writing—original draft preparation, J.L.; writing—review and editing, J.L. and J.Y.; visualization, J.L.; supervision, J.Y.; project administration, J.Y.; funding acquisition, J.Y. All authors have read and agreed to the published version of the manuscript.

Funding: This research was funded by the National Natural Science Foundation of China, grant number "41473035 and 41873036".

Data Availability Statement: Presented data are available upon request to the corresponding author.

Acknowledgments: We thank Engineer Di Zhang for her help with the apatite major element analysis and Yueheng Yang and Lei Xu for their help with the apatite trace element and Sr–Nd isotope analyses, respectively.

Conflicts of Interest: The authors declare no conflict of interest.

References

1. O'Reilly, S.Y.; Griffin, W.L. Apatite in the mantle: Implications for metasomatic processes and high heat production in Phanerozoic mantle. *Lithos* **2000**, *53*, 217–232. [CrossRef]
2. Piccoli, P.M.; Candela, P.A. Apatite in igneous systems. *Rev. Mineral. Geochem.* **2002**, *48*, 255–292. [CrossRef]
3. Harlov, D.E. Apatite: A fingerprint for Metasomatic Processes. *Elements* **2015**, *11*, 171–176. [CrossRef]
4. Bain, W.M.; Steele-MacInnis, M.; Li, K.; Li, L.; Mazdab, F.K.; Marsh, E.E. A fundamental role of carbonate-sulfate melts in the formation of iron oxide-apatite deposits. *Nat. Geosci.* **2020**, *13*, 751–757. [CrossRef]
5. Huang, X.W.; Boutroy, E.; Makvandi, S.; Beaudoin, G.; Corriveau, L.; De Toni, A.F. Trace element composition of iron oxides from IOCG and IOA deposits: Relationship to hydrothermal alteration and deposit subtypes. *Miner. Depos.* **2019**, *54*, 525–552. [CrossRef]
6. Filippelli, G.M. The global phosphorus cycle. *Rev. Mineral. Geochem.* **2002**, *48*, 391–425. [CrossRef]
7. Filippelli, G.M. The global phosphorus cycle: Past, present, and future. *Elements* **2008**, *4*, 89–95. [CrossRef]
8. Boyce, J.W.; Tomlinson, S.M.; McCubbin, F.M.; Greenwood, J.P.; Treiman, A.H. The lunar apatite paradox. *Science* **2014**, *344*, 400–402. [CrossRef]
9. Konecke, B.A.; Fiege, A.; Simon, A.C.; Holtz, F. Cryptic metasomatism during late-stage lunar magmatism implicated by sulfur in apatite. *Geology* **2017**, *45*, 739–742. [CrossRef]
10. Greenwood, J.P.; Itoh, S.; Sakamoto, N.; Warren, P.; Taylor, L.; Yurimoto, H. Hydrogen isotope ratios in lunar rocks indicate delivery of cometary water to the Moon. *Nat. Geosci.* **2011**, *4*, 79–82. [CrossRef]
11. Hughes, J.M.; Cameron, M.; Mariano, A.N. Rare-earth-element ordering and structural variations in natural rare-earth-bearing apatites. *Am. Mineral.* **1991**, *76*, 1165–1173.
12. Broom-Fendley, S.; Styles, M.T.; Appleton, J.D.; Gunn, G.; Wall, F. Evidence for dissolution-reprecipitation of apatite and preferential LREE mobility in carbonatite-derived late-stage hydrothermal processes. *Am. Mineral.* **2016**, *101*, 596–611. [CrossRef]
13. Buhn, B.; Wall, F.; Le Bas, M.J. Rare-earth element systematics of carbonatitic fluorapatites, and their significance for carbonatite magma evolution. *Contrib. Mineral. Petr.* **2001**, *141*, 572–591. [CrossRef]
14. Hornig-Kjarsgaard, I. Rare earth elements in sovitic carbonatites and their mineral phases. *J. Petrol.* **1998**, *39*, 2105–2121. [CrossRef]
15. Sha, L.K.; Chappell, B.W. Apatite chemical composition, determined by electron microprobe and laser-ablation inductively coupled plasma mass spectrometry, as a probe into granite petrogenesis. *Geochim. Cosmochim. Acta* **1999**, *63*, 3861–3881. [CrossRef]
16. Hughes, J.M.; Rakovan, J.F. Structurally robust, chemically diverse: Apatite and apatite supergroup minerals. *Elements* **2015**, *11*, 165–170. [CrossRef]
17. Pan, Y.M.; Fleet, M.E. Compositions of the apatite-group minerals: Substitution mechanisms and controlling factors. *Rev. Mineral. Geochem.* **2002**, *48*, 13–49. [CrossRef]

18. Chakhmouradian, A.R.; Reguir, E.P.; Zaitsev, A.N.; Coueslan, C.; Xu, C.; Kynicky, J.; Mumin, A.H.; Yang, P. Apatite in carbonatitic rocks: Compositional variation, zoning, element partitioning and petrogenetic significance. *Lithos* **2017**, *274*, 188–213. [CrossRef]
19. Belousova, E.A.; Griffin, W.L.; O'Reilly, S.Y.; Fisher, N.I. Igneous zircon: Trace element composition as an indicator of source rock type. *Contrib. Mineral. Petr.* **2002**, *143*, 602–622. [CrossRef]
20. Boyce, J.W.; Hervig, R.L. Magmatic degassing histories from apatite volatile stratigraphy. *Geology* **2008**, *36*, 63–66. [CrossRef]
21. Ladenburger, S.; Marks, M.A.W.; Upton, B.; Hill, P.; Wenzel, T.; Markl, G. Compositional variation of apatite from rift-related alkaline igneous rocks of the Gardar Province, South Greenland. *Am. Mineral.* **2016**, *101*, 612–626. [CrossRef]
22. Hoskin, P.W.O.; Kinny, P.D.; Wyborn, D.; Chappell, B.W. Identifying accessory mineral saturation during differentiation in granitoid magmas: An integrated approach. *J. Petrol.* **2000**, *41*, 1365–1396. [CrossRef]
23. Miles, A.J.; Graham, C.M.; Hawkesworth, C.J.; Gillespie, M.R.; Hinton, R.W.; Bromiley, G.D.; EMMAC. Apatite: A new redox proxy for silicic magmas? *Geochim. Cosmochim. Acta* **2014**, *132*, 101–119. [CrossRef]
24. Chu, M.F.; Wang, K.L.; Griffin, W.L.; Chung, S.L.; O'Reilly, S.Y.; Pearson, N.J.; Iizuka, Y. Apatite composition: Tracing petrogenetic processes in Transhimalayan granitoids. *J. Petrol.* **2009**, *50*, 1829–1855. [CrossRef]
25. Chen, W.; Simonetti, A.; Burns, P.C. A Combined geochemical and geochronological investigation of niocalite from the Oka carbonatite complex, Canada. *Can. Mineral.* **2013**, *51*, 785–800. [CrossRef]
26. Bruand, E.; Storey, C.; Fowler, M. Accessory mineral chemistry of high Ba-Sr granites from Northern Scotland: Constraints on petrogenesis and records of whole-rock signature. *J. Petrol.* **2014**, *55*, 1619–1651. [CrossRef]
27. O'Sullivan, G.; Chew, D.; Kenny, G.; Henrichs, I.; Mulligan, D. The trace element composition of apatite and its application to detrital provenance studies. *Earth-Sci. Rev.* **2020**, *201*, 103044. [CrossRef]
28. Mitchell, R.H. Peralkaline Nephelinite-natrocarbonatite immiscibility and carbonatite assimilation at Oldoinyo Lengai, Tanzania. *Contrib. Mineral. Petr.* **2009**, *158*, 589–598. [CrossRef]
29. Guzmics, T.; Mitchell, R.H.; Szabo, C.; Berkesi, M.; Milke, R.; Ratter, K. Liquid immiscibility between silicate, carbonate and sulfide melts in melt inclusions hosted in co-precipitated minerals from Kerimasi volcano (Tanzania): Evolution of carbonated nephelinitic magma. *Contrib. Mineral. Petr.* **2012**, *164*, 101–122. [CrossRef]
30. Beccaluva, L.; Barbieri, M.; Born, H.; Brotzu, P.; Coltorti, M.; Conte, A.; Garbarino, C.; Gomes, C.B.; Macciotta, G.; Morbidelli, L.; et al. Fractional crystallization and liquid immiscibility processes in the alkaline-carbonatite complex of Juquia (Sao-Paulo, Brazil). *J. Petrol.* **1992**, *33*, 1371–1404. [CrossRef]
31. Lee, W.J.; Wyllie, P.J. Processes of crustal carbonatite formation by liquid immiscibility and differentiation, elucidated by model systems. *J. Petrol.* **1998**, *39*, 2005–2013. [CrossRef]
32. Dasgupta, R.; Hirschmann, M.M.; Stalker, K. Immiscible transition from carbonate-rich to silicate-rich melts in the 3 GPa melting interval of eclogite plus CO_2 and genesis of silica-undersaturated ocean island lavas. *J. Petrol.* **2006**, *47*, 647–671. [CrossRef]
33. Hammouda, T. High-pressure melting of carbonated eclogite and experimental constraints on carbon recycling and storage in the mantle. *Earth Planet. Sci. Lett.* **2003**, *214*, 357–368. [CrossRef]
34. Thomsen, T.B.; Schmidt, M.W. Melting of carbonated pelites at 2.5–5.0 GPa, silicate-carbonatite liquid immiscibility, and potassium-carbon metasomatism of the mantle. *Earth Planet. Sci. Lett.* **2008**, *267*, 17–31. [CrossRef]
35. Chakhmouradian, A.R.; Mumin, A.H.; Demeny, A.; Elliott, B. Postorogenic carbonatites at Eden Lake, Trans-Hudson Orogen (northern Manitoba, Canada): Geological setting, mineralogy and geochemistry. *Lithos* **2008**, *103*, 503–526. [CrossRef]
36. Conceicao, F.T.; Vasconcelos, P.M.; Godoy, L.H.; Navarro, G.R.B. $^{49}Ar/^{39}Ar$ geochronological evidence for multiple magmatic events during the emplacement of Tapira alkaline-carbonatite complex, Minas Gerais, Brazil. *J. S. Am. Earth Sci.* **2020**, *97*, 102416. [CrossRef]
37. Xu, C.; Campbell, I.H.; Allen, C.M.; Chen, Y.J.; Huang, Z.L.; Qi, L.; Zhang, G.S.; Yan, Z.F. U-Pb zircon age, geochemical and isotopic characteristics of carbonatite and syenite complexes from the Shaxiongdong, China. *Lithos* **2008**, *105*, 118–128. [CrossRef]
38. Chen, W.; Lu, J.; Jiang, S.Y.; Ying, Y.C.; Liu, Y.S. Radiogenic Pb reservoir contributes to the rare earth element (REE) enrichment in South Qinling carbonatites. *Chem. Geol.* **2018**, *494*, 80–95. [CrossRef]
39. Su, J.H.; Zhao, X.F.; Li, X.C.; Hu, W.; Chen, W.; Sleak, P. Unmixing of REE-Nb enriched carbonatites after incremental fractionation of alkaline magmas in the Shaxiongdong complex, Central China. *Lithos* **2022**, *416*, 106651. [CrossRef]
40. Gervasoni, F.; Klemme, S.; Rohrbach, A.; Grutzner, T.; Berndt, J. Experimental constraints on the stability of baddeleyite and zircon in carbonate- and silicate-carbonate melts. *Am. Mineral.* **2017**, *102*, 860–866. [CrossRef]
41. Mitchell, R.; Chudy, T.; McFarlane, C.R.M.; Wu, F.Y. Trace element and isotopic composition of apatite in carbonatites from the Blue River area (British Columbia, Canada) and mineralogy of associated silicate rocks. *Lithos* **2017**, *286*, 75–91. [CrossRef]
42. Brassinnes, S.; Balaganskaya, E.; Demaiffe, D. Magmatic evolution of the differentiated ultramafic, alkaline and carbonatite intrusion of vuoriyarvi (Kola Peninsula, Russia). A LA-ICP-MS study of apatite. *Lithos* **2005**, *85*, 76–92. [CrossRef]
43. Dong, Y.P.; Santosh, M. Tectonic architecture and multiple orogeny of the Qinling Orogenic Belt, Central China. *Gondwana Res.* **2016**, *29*, 1–40. [CrossRef]
44. Dong, Y.P.; Zhang, G.W.; Neubauer, F.; Liu, X.M.; Genser, J.; Hauzenberger, C. Tectonic evolution of the Qinling orogen, China: Review and synthesis. *J. Asian Earth Sci.* **2011**, *41*, 213–237. [CrossRef]
45. Meng, Q.R.; Zhang, G.W. Geologic framework and tectonic evolution of the Qinling orogen, central China. *Tectonophysics* **2000**, *323*, 183–196. [CrossRef]

46. Nie, H.; Wan, X.; Zhang, H.; He, J.F.; Hou, Z.H.; Siebel, W.; Chen, F.K. Ordovician and Triassic mafic dykes in the Wudang terrane: Evidence for opening and closure of the South Qinling ocean basin, central China. *Lithos* **2016**, *266*, 1–15. [CrossRef]
47. Ling, W.L.; Ren, B.F.; Duan, R.C.; Liu, X.M.; Mao, X.W.; Peng, L.H.; Liu, Z.X.; Cheng, J.P.; Yang, H.M. Timing of the Wudangshan, Yaolinghe volcanic sequences and mafic sills in South Qinling: U-Pb zircon geochronology and tectonic implication. *Chin. Sci. Bull.* **2008**, *53*, 2192–2199. [CrossRef]
48. Su, J.H.; Zhao, X.F.; Li, X.C.; Su, Z.K.; Liu, R.; Qin, Z.J.; Chen, M. Fingerprinting REE mineralization and hydrothermal remobilization history of the carbonatite-alkaline complexes, Central China: Constraints from in situ elemental and isotopic analyses of phosphate minerals. *Am. Mineral.* **2021**, *106*, 1545–1558. [CrossRef]
49. Wu, S.T.; Karius, V.; Schmidt, B.C.; Simon, K.; Worner, G. Comparison of ultrafine powder pellet and flux-free fusion glass for bulk analysis of granitoids by laser ablation-inductively coupled plasma-mass spectrometry. *Geostand. Geoanal. Res.* **2018**, *42*, 575–591. [CrossRef]
50. Yang, Y.H.; Sun, J.F.; Xie, L.W.; Fan, H.R.; Wu, F.Y. In situ Nd isotopic measurement of natural geological materials by LA-MC-ICPMS. *Chin. Sci. Bull.* **2008**, *53*, 1062–1070. [CrossRef]
51. Yang, Y.H.; Wu, F.Y.; Wilde, S.A.; Liu, X.M.; Zhang, Y.B.; Xie, L.W.; Yang, J.H. In situ perovskite Sr–Nd isotopic constraints on the petrogenesis of the Ordovician Mengyin kimberlites in the North China Craton. *Chem. Geol.* **2009**, *264*, 24–42. [CrossRef]
52. Yang, Y.H.; Wu, F.Y.; Yang, J.H.; Chew, D.M.; Xie, L.W.; Chu, Z.Y.; Zhang, Y.B.; Huang, C. Sr and Nd isotopic compositions of apatite reference materials used in U-Th-Pb geochronology. *Chem. Geol.* **2014**, *385*, 35–55. [CrossRef]
53. McFarlane, C.R.M.; McCulloch, M.T. Coupling of in-situ Sm-Nd systematics and U-Pb dating of monazite and allanite with applications to crustal evolution studies. *Chem. Geol.* **2007**, *245*, 45–60. [CrossRef]
54. Wu, Y.C.; Yang, Y.H.; Wu, F.Y.; Yang, J.H. Error calculation of radiogenic geochemical parameters in isotopic geology: A case study of Hf-Nd-Sr isotopes. *Geochimica* **2015**, *44*, 600–607.
55. Anders, E.; Grevesse, N. Abundances of the Elements - Meteoritic and Solar. *Geochim. Cosmochim. Acta* **1989**, *53*, 197–214. [CrossRef]
56. Sun, W.; McDonough, W. Chemical and isotopic systematics of oceanic basalts: Implications for mantle composition and processes. *Geol. Soc. Lond. Spec. Publ.* **1989**, *42*, 313–345. [CrossRef]
57. Bell, K.; Blenkinsop, J. Nd and Sr Isotopic Compositions of East-African carbonatites - Implications for mantle heterogeneity. *Geology* **1987**, *15*, 99–102. [CrossRef]
58. Bell, K.; Tilton, G.R. Nd, Pb and Sr isotopic compositions of east African carbonatites: Evidence for mantle mixing and plume inhomogeneity. *J. Petrol.* **2001**, *42*, 1927–1945. [CrossRef]
59. Bell, K. Radiogenic isotope constraints on relationships between carbonatites and associated silicate rocks—A brief review. *J. Petrol.* **1998**, *39*, 1987–1996. [CrossRef]
60. Zhang, C.L.; Zhou, D.W.; Jin, H.L.; Han, S.; Liu, Y.Y. Study on the Sr, Nd, Pb and O isotopes of basic dyke swarms in the Wudang block and basic valcanics of the Yaolinghe Group. *Acta Petrol. Sin.* **1999**, *15*, 430–437.
61. Zhao, G.C.; Hu, J.M.; Meng, Q.R. Geochemistry of the basic sills in the western Wudang block: The evidences of the Paleozoic underplating in South Qinling. *Acta Petrol. Sin.* **2003**, *19*, 612–622.
62. Chen, J.F.; Jahn, B.M. Crustal evolution of southeastern China: Nd and Sr isotopic evidence. *Tectonophysics* **1998**, *284*, 101–133. [CrossRef]
63. Gao, S.; Ling, W.L.; Qiu, Y.M.; Lian, Z.; Hartmann, G.; Simon, K. Contrasting geochemical and Sm-Nd isotopic compositions of Archean metasediments from the Kongling high-grade terrain of the Yangtze craton: Evidence for cratonic evolution and redistribution of REE during crustal anatexis. *Geochim. Cosmochim. Acta* **1999**, *63*, 2071–2088. [CrossRef]
64. Ma, C.Q.; Ehlers, C.; Xu, C.H.; Li, Z.C.; Yang, K.G. The roots of the Dabieshan ultrahigh-pressure metamorphic terrane: Constraints from geochemistry and Nd-Sr isotope systematics. *Precambrian Res.* **2000**, *102*, 279–301. [CrossRef]
65. Wang, R.R.; Xu, Z.Q.; Santosh, M.; Liang, F.H.; Fu, X.H. Petrogenesis and tectonic implications of the Early Paleozoic intermediate and mafic intrusions in the South Qinling Belt, Central China: Constraints from geochemistry, zircon U-Pb geochronology and Hf isotopes. *Tectonophysics* **2017**, *712*, 270–288. [CrossRef]
66. Eby, G.N. Abundance and distribution of rare-earth elements and yttrium in rocks and minerals of Oka carbonatite complex, Quebec. *Geochim. Cosmochim. Acta* **1975**, *39*, 597–620. [CrossRef]
67. Webster, J.D.; Piccoli, P.M. Magmatic apatite: A powerful, yet deceptive, mineral. *Elements* **2015**, *11*, 177–182. [CrossRef]
68. Sun, J.F.; Yang, J.H.; Zhang, J.H.; Yang, Y.H.; Zhu, Y.S. Apatite geochemical and Sr–Nd isotopic insights into granitoid petrogenesis. *Chem. Geol.* **2021**, *566*, 12. [CrossRef]
69. Sun, C.Y.; Cawood, P.A.; Xu, W.L.; Zhang, X.M.; Tang, J.; Li, Y.; Sun, Z.X.; Xu, T. In situ geochemical composition of apatite in granitoids from the eastern Central Asian Orogenic Belt: A window into petrogenesis. *Geochim. Cosmochim. Acta* **2022**, *317*, 552–573. [CrossRef]
70. Lu, J.; Chen, W.; Ying, Y.C.; Jiang, S.Y.; Zhao, K.D. Apatite texture and trace element chemistry of carbonatite-related REE deposits in China: Implications for petrogenesis. *Lithos* **2021**, *398*, 106276. [CrossRef]
71. Broom-Fendley, S.; Brady, A.E.; Wall, F.; Gunn, G.; Dawes, W. REE minerals at the Songwe Hill carbonatite, Malawi: HREE-enrichment in late-stage apatite. *Ore Geol. Rev.* **2017**, *81*, 23–41. [CrossRef]

72. Sheard, E.R.; Williams-Jones, A.E.; Heiligmann, M.; Pederson, C.; Trueman, D.L. Controls on the concentration of zirconium, niobium, and the rare earth elements in the Thor Lake rare metal deposit, Northwest Territories, Canada. *Econ. Geol.* **2012**, *107*, 81–104. [CrossRef]
73. Chakhmouradian, A.R.; Reguir, E.P.; Kressall, R.D.; Crozier, J.; Pisiak, L.K.; Sidhu, R.; Yang, P. Carbonatite-hosted niobium deposit at Aley, northern British Columbia (Canada): Mineralogy, geochemistry and petrogenesis. *Ore Geol. Rev.* **2015**, *64*, 642–666. [CrossRef]
74. Zaitsev, A.N.; Chakhmouradian, A.R. Calcite-amphibole-clinopyroxene rock from the Afrikanda Complex, Kola Peninsula, Russia: Mineralogy and a possible link to carbonatites. II. Oxysalt minerals. *Can. Mineral.* **2002**, *40*, 103–120. [CrossRef]
75. Migdisov, A.A.; Williams-Jones, A.E.; Wagner, T. An experimental study of the solubility and speciation of the rare earth elements (III) in fluoride- and chloride-bearing aqueous solutions at temperatures up to 300 degrees C. *Geochim. Cosmochim. Acta* **2009**, *73*, 7087–7109. [CrossRef]
76. Williams-Jones, A.E.; Palmer, D.A.S. The evolution of aqueous-carbonic fluids in the Amba Dongar carbonatite, India: Implications for fenitisation. *Chem. Geol.* **2002**, *185*, 283–301. [CrossRef]
77. Williams-Jones, A.E.; Migdisov, A.A.; Samson, I.M. Hydrothermal mobilisation of the rare earth elements—A tale of "Ceria" and "Yttria". *Elements* **2012**, *8*, 355–360. [CrossRef]
78. Xie, Y.L.; Hou, Z.Q.; Yin, S.P.; Dominy, S.C.; Xu, J.H.; Tian, S.H.; Xu, W.Y. Continuous carbonatitic melt-fluid evolution of a REE mineralization system: Evidence from inclusions in the Maoniuping REE Deposit, Western Sichuan, China. *Ore Geol. Rev.* **2009**, *36*, 90–105. [CrossRef]
79. Xie, Y.L.; Li, Y.X.; Hou, Z.Q.; Cooke, D.R.; Danyushevsky, L.; Dominy, S.C.; Yin, S.P. A model for carbonatite hosted REE mineralisation—The Mianning-Dechang REF belt, Western Sichuan Province, China. *Ore Geol. Rev.* **2015**, *70*, 595–612. [CrossRef]
80. Chen, W.; Simonetti, A. In-situ determination of major and trace elements in calcite and apatite, and U-Pb ages of apatite from the Oka carbonatite complex: Insights into a complex crystallization history. *Chem. Geol.* **2013**, *353*, 151–172. [CrossRef]
81. Xu, C.; Kynicky, J.; Chakhmouradian, A.R.; Campbell, I.H.; Allen, C.M. Trace-element modeling of the magmatic evolution of rare-earth-rich carbonatite from the Miaoya deposit, Central China. *Lithos* **2010**, *118*, 145–155. [CrossRef]
82. Zhang, D.X.; Liu, Y.; Pan, J.Q.; Dai, T.G.; Bayless, R.C. Mineralogical and geochemical characteristics of the Miaoya REE prospect, Qinling orogenic Belt, China: Insights from Sr–Nd-C-O isotopes and LA-ICP-MS mineral chemistry. *Ore Geol. Rev.* **2019**, *110*, 102932. [CrossRef]
83. Watson, E.B.; Green, T.H. Apatite Liquid partition-coefficients for the rare-Earth elements and strontium. *Earth Planet. Sci. Lett.* **1981**, *56*, 405–421. [CrossRef]
84. Klemme, S.; Dalpe, C. Trace-element partitioning between apatite and carbonatite melt. *Am. Mineral.* **2003**, *88*, 639–646. [CrossRef]
85. Hammouda, T.; Chantel, J.; Devidal, J.L. Apatite solubility in carbonatitic liquids and trace element partitioning between apatite and carbonatite at high pressure. *Geochim. Cosmochim. Acta* **2010**, *74*, 7220–7235. [CrossRef]
86. Guzmics, T.; Zajacz, Z.; Kodolanyi, J.; Halter, W.; Szabo, C. LA-ICP-MS study of apatite- and K feldspar-hosted primary carbonatite melt inclusions in clinopyroxenite xenoliths from lamprophyres, Hungary: Implications for significance of carbonatite melts in the Earth's mantle. *Geochim. Cosmochim. Acta* **2008**, *72*, 1864–1886. [CrossRef]
87. Prowatke, S.; Klemme, S. Trace element partitioning between apatite and silicate melts. *Geochim. Cosmochim. Acta* **2006**, *70*, 4513–4527. [CrossRef]
88. Barth, S.; Oberli, F.; Meier, M. Th-Pb Versus U-Pb Isotope systematics in allanite—From co-genetic rhyolite and granodiorite - Implications for geochronology. *Earth Planet. Sci. Lett.* **1994**, *124*, 149–159. [CrossRef]
89. Fujimaki, H. Partition-coefficients of Hf, Zr, and REE between zircon, apatite, and liquid. *Contrib. Mineral. Petr.* **1986**, *94*, 42–45. [CrossRef]
90. Tang, M.; Wang, X.L.; Xu, X.S.; Zhu, C.; Cheng, T.; Yu, Y. Neoproterozoic subducted materials in the generation of Mesozoic Luzong volcanic rocks: Evidence from apatite geochemistry and Hf-Nd isotopic decoupling. *Gondwana Res.* **2012**, *21*, 266–280. [CrossRef]
91. Tollari, N.; Barnes, S.J.; Cox, R.A.; Nabil, H. Trace element concentrations in apatites from the Sept-Iles Intrusive Suite, Canada—Implications for the genesis of nelsonites. *Chem. Geol.* **2008**, *252*, 180–190. [CrossRef]
92. Shannon, R.D. Revised effective ionic-radii and systematic studies of interatomic distances in halides and chalcogenides. *Acta Crystallogr. A* **1976**, *32*, 751–767. [CrossRef]
93. Cao, M.J.; Li, G.M.; Qin, K.Z.; Seitmuratova, E.Y.; Liu, Y.S. Major and trace element characteristics of apatites in granitoids from Central Kazakhstan: Implications for petrogenesis and mineralization. *Resour. Geol.* **2012**, *62*, 63–83. [CrossRef]
94. He, H.L.; Wang, Y.Q.; Bao, Z.A.; George, P.M.; Veni, S.; Sajeev, K.; Guo, J.H.; Zhai, M.G.; Lai, C.K. Role of magma injection and mixing in the formation of chromitite in Archean anorthosites: Evidence from the Sittampundi Complex, southern India. *Precambrian Res.* **2020**, *350*, 105914. [CrossRef]
95. Nandedkar, R.H.; Hurlimann, N.; Ulmer, P.; Muntener, O. Amphibole-melt trace element partitioning of fractionating calc-alkaline magmas in the lower crust: An experimental study. *Contrib. Mineral. Petr.* **2016**, *171*, 71. [CrossRef]
96. Tiepolo, M.; Vannucci, R.; Oberti, R.; Foley, S.; Bottazzi, P.; Zanetti, A. Nb and Ta incorporation and fractionation in titanian pargasite and kaersutite: Crystal-chemical constraints and implications for natural systems. *Earth Planet. Sci. Lett.* **2000**, *176*, 185–201. [CrossRef]

97. Tiepolo, M.; Vannucci, R.; Bottazzi, P.; Oberti, R.; Zanetti, A.; Foley, S. Partitioning of rare earth elements, Y, Th, U, and Pb between pargasite, kaersutite, and basanite to trachyte melts: Implications for percolated and veined mantle. *Geochem. Geophy. Geosy.* **2000**, *1*. [CrossRef]
98. Zhang, F.Y.; Lai, S.C.; Qin, J.F.; Zhu, R.Z.; Zhao, S.W.; Zhu, Y.; Yang, H. Vein-plus-wall rock melting model for the origin of Early Paleozoic alkali diabases in the South Qinling Belt, Central China. *Lithos* **2020**, *370*, 105619. [CrossRef]
99. Zhang, C.L.; Gao, S.; Yuan, H.L.; Zhang, G.W.; Yan, Y.X.; Luo, J.L.; Luo, J.H. Sr–Nd–Pb isotopes of the early Paleozoic mafic-ultramafic dykes and basalts from South Qinling belt and their implications for mantle composition. *Sci. China Ser. D* **2007**, *50*, 1293–1301. [CrossRef]
100. Xia, L.Q.; Xia, Z.C.; Zhang, C.; Xu, X.Y. *Geochemistry of Alkali Basic, Ultrabasic Subvolcanic Complex from Northern Daba Mountains, China*; Geological Publishing House: Beijing, China, 1994.
101. Xu, X.Y.; Huang, Y.H.; Xia, L.Q.; Xia, Z.C. Phlogopite-amphibole-pyroxenite xenoliths in Langao, Shanxi Province: Evidence for mantle metasomatism. *Acta Petrol. Sin.* **1997**, *13*, 2–14.
102. Huang, Y.H. Mineralogical characteristics of phlogopite-amphibole-pyroxenite mantle xenoliths included in the alkali mafic-ultramafic subvolcanic complex from Langao county China. *Acta Petrol. Sin.* **1993**, *9*, 367–378.
103. Ernst, R.E.; Bell, K. Large igneous provinces (LIPs) and carbonatites. *Mineral. Petrol.* **2010**, *98*, 55–76. [CrossRef]
104. Hofmann, A.W. Mantle geochemistry: The message from oceanic volcanism. *Nature* **1997**, *385*, 219–229. [CrossRef]
105. Pilet, S.; Baker, M.B.; Stolper, E.M. Metasomatized lithosphere and the origin of alkaline lavas. *Science* **2008**, *320*, 916–919. [CrossRef]
106. Pilet, S.; Baker, M.B.; Muntener, O.; Stolper, E.M. Monte Carlo simulations of metasomatic enrichment in the lithosphere and implications for the source of alkaline basalts. *J. Petrol.* **2011**, *52*, 1415–1442. [CrossRef]
107. Weiss, Y.; Class, C.; Goldstein, S.L.; Hanyu, T. Key new pieces of the HIMU puzzle from olivines and diamond inclusions. *Nature* **2016**, *537*, 666–670. [CrossRef]
108. Castillo, P.R. A proposed new approach and unified solution to old Pb paradoxes. *Lithos* **2016**, *252*, 32–40. [CrossRef]
109. Castillo, P.R. The recycling of marine carbonates and sources of HIMU and FOZO ocean island basalts. *Lithos* **2015**, *216*, 254–263. [CrossRef]
110. Zhang, Y.X.; Ni, H.W.; Chen, Y. Diffusion data in silicate melts. *Rev. Mineral. Geochem.* **2010**, *72*, 311–408. [CrossRef]
111. Li, W.Y.; Teng, F.Z.; Xiao, Y.L.; Huang, J.A. High-temperature inter-mineral magnesium isotope fractionation in eclogite from the Dabie orogen, China. *Earth Planet. Sci. Lett.* **2011**, *304*, 224–230. [CrossRef]